ACS Catalysis

pubs.acs.org/acscatalysis Research Article

Orchestrating Cluster-Level Atomic Assemblies for Hydrogen/Solvent-Free Plastic Upcycling

Fan Mo, Chuan Yin, Ting Ma, Yue Yang, Kaixuan Wang, Xi Chen, Ningqiang Zhang, Wei Yu,* and Haibo Li*

Cite This: *ACS Catal.* 2026, 16, 2194−2208 Read Online

ACCESS | Metrics & More | Article Recommendations | Supporting Information

ABSTRACT: The size of supported metal species plays a critical role in catalytic activity, yet the atomic-scale structure sensitivity in hydrogen- and solvent-free thermal polymer upcycling has not been fully explored. This study investigated the relationship between the atomic configuration and upcycling efficiency, aiming to optimize the yield of valuable aromatics. High-order Ru atomic clusters (ACs) with optimal coordination incorporated into hydrogen-form Zeolite Socony Mobil-5-300H (HZSM-5-300H) showed superior low-density polyethylene (LDPE) conversion (62.93% vs 41.61%), better aromatic selectivity (70.43% vs 48.43%), and more favorable economic viability compared to low-order Ru ACs with isolated atomic sites on HZSM-5-300H. Structural and performance analysis revealed that the Ru assembly was a dominant factor in plastic upcycling, overshadowing the contributions of other components. The increased conversion was attributed to the optimal adsorption energy of intermediates and the enhanced dehydrogenation capacity of high-order Ru ACs, improving the feasibility of subsequent steps. Distinguished aromatic yield was achieved due to efficient dehydro-aromatization and hydrogen migration while minimizing rehydrogenation of aromatics and maintaining appropriate H* binding capacity. The metal−acid balance for 0.5 wt % Ru/300H (i.e., high-order Ru ACs) was better optimized for C−C cleavage compared to 0.2 wt % Ru/300H (i.e., low-order Ru ACs), leading to a significant increase in turnover frequency (TOF) for aromatic yield from cyclohexane dehydro-aromatization, rising from 296.56 $\mu M \cdot mg^{-1}$ Ru·h^{-1} to 544.34 $\mu M \cdot mg^{-1}$ Ru·h^{-1}. The scalability of this approach can be extended to various systems, including different metals, supports, and acidities. Overall, this study highlights the advantages of high-order Ru ACs over low-order Ru ACs in hydrogen- and solvent-free waste plastic upcycling, offering insights into the development of efficient, cost-effective catalysts for polymer recycling.

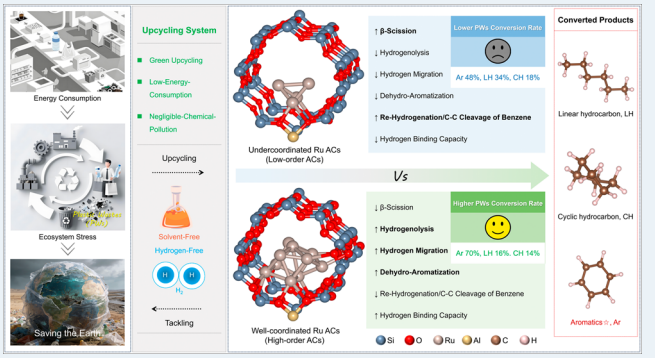

KEYWORDS: *atomic assembly degree, discrete metal sites, plastic upcycling, dehydro-aromatization, hydrogen migration*

INTRODUCTION

The efficient recycling of plastics (with an annual production exceeding 400 million tons) represents a paramount challenge in mitigating global plastic pollution, which poses significant threats to wildlife and biodiversity, alongside the enormous resource waste typically downcycled through mechanical processing, landfill disposal, and incineration.[1−5] Although current recycling methodologies—particularly hydrogen-free and solvent-free upcycling techniques—have made notable strides, they remain beset by substantial limitations, which are reflected in both the insufficient atomic utilization of the recycling processes and the lack of a comprehensive understanding of the underlying mechanistic details. In recent years, the critical role of atomic-level catalyst structures in modulating the reaction efficiency and selectivity has become increasingly apparent. For instance, the catalytic performance of Ru single atoms (SAs) was significantly enhanced through the construction of Ru SA-loaded Co nanoparticles (NPs), which facilitated the synergistic coupling of Ru-mediated hydrogenation with Co-promoted C−C bond cleavage. Similarly, Ru SAs acted as hydrogenation sites, preventing excessive carbon chain cleavage in Co NPs, thereby improving the hydrogenolysis selectivity of Co−Co sites.[6] Moreover, in the context of high-entropy intermetallic compounds (HEIs), a lattice compensation strategy—incorporating larger atomic radius elements such as Bi and Mo into the B-site of the FePt parent metal—was employed to mitigate phase segregation induced by entropy reduction. This resulted in the formation of an L10-(PtIr)(FeMoBi) HEI with both long-range atomic

Received: September 19, 2025
Revised: January 13, 2026
Accepted: January 15, 2026
Published: January 20, 2026

https://doi.org/10.1021/acscatal.5c06674
ACS Catal. 2026, 16, 2194−2208

ordering and short-range atomic disorder, which demonstrated exceptional electrocatalytic performance for the ethylene glycol oxidation to glycolic acid reaction.[7] Despite these advances, the precise influence of atomic structural arrangements on complex processes, such as the hydrogen-free and solvent-free recycling of plastics, remains underexplored.

The atomic structure, particularly the aggregation state of atoms—encompassing the spatial organization and ordering of atomic constituents within a material—has been firmly established as a pivotal factor governing reaction efficiency.[5,8,9] For example, by varying the atomic number of Fe, from single Fe atoms to diatomic and triatomic clusters, a volcano-shaped correlation was established between the Fe atom number and sulfur reduction reaction (SRR) activity, with the diatomic Fe configuration exhibiting the optimal catalytic performance.[10] In a similar vein, the catalytic performance of Ru NPs was found to be inferior to that of Ru SA-loaded CoAlO catalysts, with the latter displaying enhanced interaction between Ru SAs and plastic substrates due to a shift in the d-band center of Ru SAs toward the Fermi level, thereby improving catalytic activity.[11] Notably, when atoms aggregate into ordered clusters, the density and stability of surface-active sites can differ markedly from disordered or loosely aggregated configurations, with such structural differences potentially modulating the reaction mechanisms and, consequently, the rate and selectivity of the catalytic processes. However, a systematic investigation into how the aggregation states of atomic clusters (ACs) influence the efficiency and selectivity of plastic upcycling processes remains a crucial gap in the current body of research.

Building on these advances, this study focuses on the catalytic mechanisms of plastic upcycling under hydrogen-free and solvent-free conditions, specifically investigating the catalytic performance of 0.2R/HZSM-5-300H (0.2*R*/300H, low-order Ru ACs with excessively isolated Ru sites) and 0.5*R*/300H systems (0.5*R*/300H, high-order Ru ACs with discrete Ru sites). By examining how atomic aggregation states influenced the reaction efficiency and selectivity, this work aimed to elucidate the role of atomic structure in optimizing the recycling of plastics. The results showed that the high-order Ru ACs significantly enhanced both the conversion (62.93% vs 41.61%) and aromatic selectivity (70.43% vs 48.43%). This improvement can be attributed to minimized side reactions, including β-scission and rehydrogenation of aromatics, coupled with enhanced dehydrogenation, cyclization (significant optimization of hydrogen migration energy barrier), and dehydro-aromatization efficiencies (significant optimization of the dehydrogenation energy barrier). Particularly, the turnover frequency (TOF) for cyclohexane dehydro-aromatization can be increased to 544.34 $\mu M\cdot_{mg}Ru^{1-}\cdot h^{-1}$ for 0.5*R*/300H, compared to 296.56 $\mu M\cdot_{mg}Ru^{1-}\cdot h^{-1}$ for 0.2*R*/300H. The industrial simulation results showed that the 0.5*R*/300H configuration had significantly better economic feasibility than the 0.2*R*/300H, with a higher return on investment (ROI) of 30.06%, a shorter payback period (PBP) of 2.66 years, and an internal rate of return (IRR) of 16%, all without depreciation. Furthermore, the net present value (NPV) was positive at \$1,778,301.25 over 5 years, also without depreciation. In contrast, the 0.2*R*/300H configuration reported a negative annual gross profit of -\$2453851.7, without depreciation. The insights gained from this research are expected to provide a deeper understanding of how atomic-level adjustments in catalyst design can enhance the sustainability and effectiveness of plastic upcycling, thereby contributing to the development of more efficient, environmentally friendly recycling technologies.

MATERIALS AND METHODS

Catalyst Preparation

The Ru/HZSM-5-300H (denoted as XR/300H) catalysts were synthesized by using a precise impregnation method. In a typical procedure, a small volume of solvent (deionized water, 10−15 mL) containing the metal precursor ($RuCl_3\cdot xH_2O$, detailed amounts summarized in Table S1) was added to 10 g of HZSM-5 support. Subsequently, the quasi-dry powders were subjected to thermal treatment under a 5% H_2/Ar atmosphere in a tube furnace at 450 °C for 120 min (Figure S1).

Similar strategies were used to synthesize serial Ir/HZSM-5-300H (denoted as XI/300H), Ru/HZSM-5-150H (denoted as XR/150H), Ru/HZSM-5-75H (denoted as XR/75H), Ru/Hβ-150H (denoted as XR/Hβ), and Ru/Al_2O_3 (denoted as XR/Al; the volume of solution containing the metal precursor was 6−8 mL). The detailed additive amounts are summarized in Table S1. Note that the reference material HZSM-5 underwent the same fabrication procedure except for the addition of $RuCl_3\cdot xH_2O$.

The metal loadings were verified by inductively coupled plasma mass spectrometry (ICP-MS, Table S2). Note that the rationality for metal selection is supplemented in Supporting Information (section: The Rationality for Metal Selection).

Plastic Upcycling

The upcycling of plastics was conducted in a 300 rpm stirred 50 mL stainless steel reactor at 280 °C for 24 h. In a typical experiment, the reactor was purged with pure Ar for 10 min to remove any residual air following the addition of 500 mg of catalyst and 5.00 g of plastic. The autoclave was then pressurized with 2.0 MPa of Ar at room temperature.

Following completion of the upcycling reaction, the gaseous products were introduced into a gas sampling bag. Subsequently, the liquid and solid products were combined with 50 mL of hot dichloromethane and transferred to a 50 mL centrifuge tube. The resultant mixture was subjected to centrifugation at 19,760*g* × for 10 min to separate the liquid and solid phases.

The gas weight was determined by measuring the mass differences of the reactor before and after the reaction. The yield of insoluble hydrocarbons was determined by subtracting the initial mass of the catalyst from the total mass of the recovered solid. The soluble hydrocarbons were recovered by evaporation overnight at 0.1 Torr, followed by weighing to determine the liquid yield.[12] The mass balance in all catalytic tests exceeded 90%. The unaccounted mass primarily consisted of the leaking of gaseous products and volatile components from the liquid-phase products that escape during the measurement process rather than coke.

The mass calculation formulas can be summarized as follows:[13]

$$m_{\text{gaseous hydrocarbons}} = m_{\text{reactor, before the reaction}} - m_{\text{reactor, after the reaction}}$$

$$m_{\text{solid hydrocarbons}} = m_{\text{solid product}} - m_{\text{added catalyst}}$$

$$m_{\text{liquid hydrocarbons}} = m_{\text{soluble hydrocarbon recovered from solid product}}$$

Gaseous products (i.e., H_2 and C_1 to C_7 hydrocarbons) were quantitatively determined by a gas chromatograph (8890 GC System, Agilent). H_2 was analyzed using combined packed columns (i.e., MolSieve 5A and HayeSep Q) with a TCD (N_2 carrier gas). Gaseous C_1 to C_7 hydrocarbons were analyzed by using an Al_2O_3 capillary column (HP-AL/S) with a flame ionization detector (FID, He carrier gas). Hydrogen, methane, ethane, propane, butane, pentane, isopentane, and hexane were used as external standard gases.

The detailed procedures can be listed as follows:

Gaseous hydrocarbons were introduced into the gas chromatography−mass spectrometry (GC−MS) system using valve injection (0.25 mL of quantitative ring) at a split ratio of 65:1. Hydrocarbons were resolved using an HP-AL/S capillary column (length: 30 m; diameter: 0.25 mm; film thickness: 5 μm; Agilent), with high-purity

https://doi.org/10.1021/acscatal.5c06674
ACS Catal. 2026, 16, 2194−2208

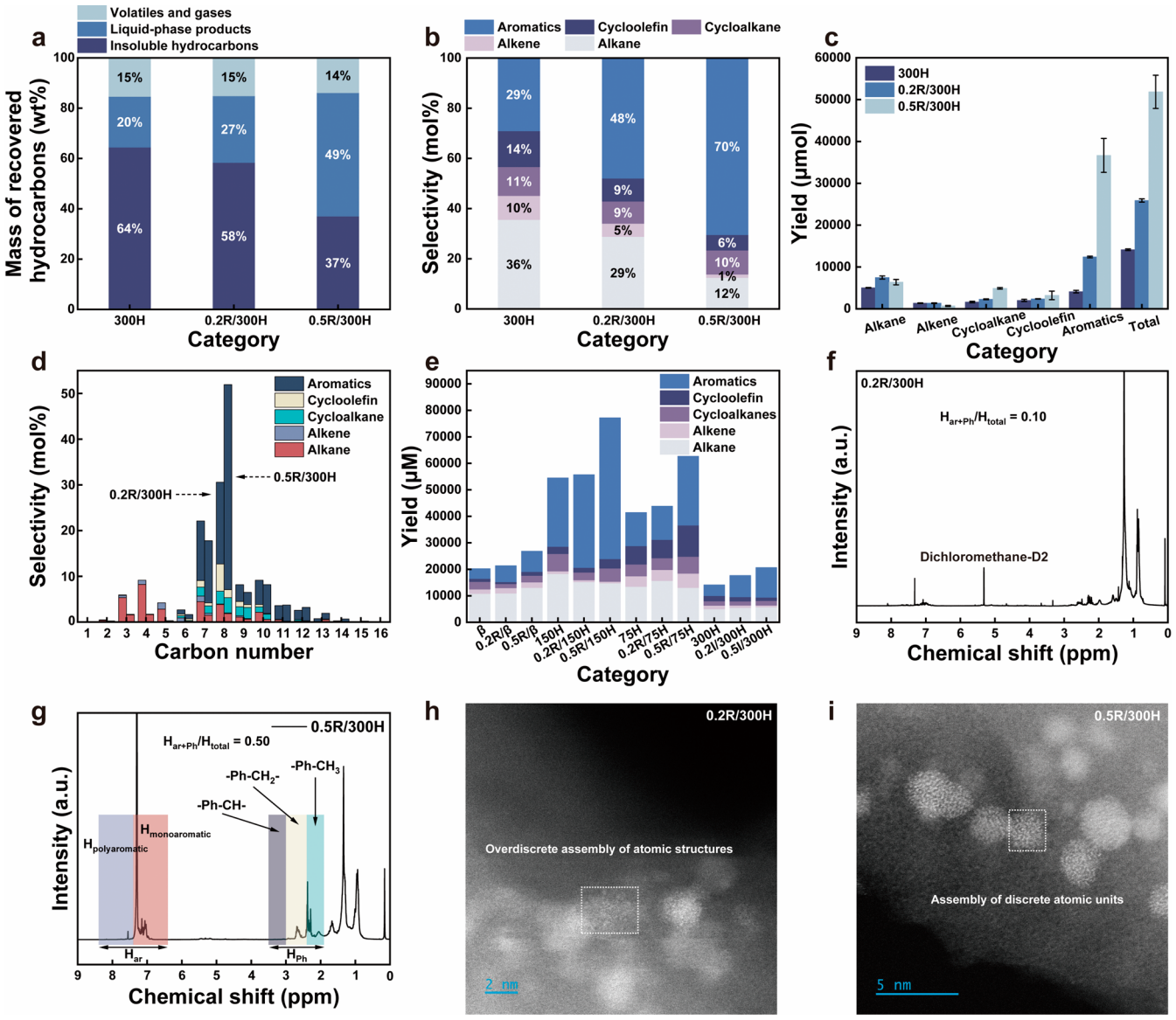

Figure 1. Elucidation of the correlation between LDPE upcycling properties and metal loadings. (a) Selectivity of volatiles/gases, liquid-phase products, and insoluble hydrocarbons in 300H, 0.2*R*/300H, and 0.5*R*/300H/LDPE/H_2-free/solvent-free systems. (b) Selectivity of alkanes, alkenes, cycloalkanes, cycloolefins, and aromatic products in 300H, 0.2*R*/300H, and 0.5*R*/300H/LDPE/H_2-free/solvent-free systems. (c) Molar yields of products in 300H, 0.2*R*/300H, and 0.5*R*/300H/LDPE/H_2-free/solvent-free systems. (d) Detailed hydrocarbon selectivity of alkanes, alkenes, cycloalkanes, cycloolefins, and aromatics with varying carbon numbers. (e) Determined molar quantities of products from LDPE upcycling mediated by metal Ru-loaded Hβ (β), HZSM-5-150H (150H), HZSM-5-75H (75H), and metal Ir-loaded 300H. (f) The ^{1}H NMR spectra of the chloroform-soluble product obtained from the hydrogen/solvent-free depolymerization of LDPE by 0.2*R*/300H. (g) The ^{1}H NMR spectra of the chloroform-soluble product obtained from the hydrogen/solvent-free depolymerization of LDPE by 0.5*R*/300H. (h) The AC-HAADF-STEM image for low-order Ru ACs in 0.2*R*/300H. (i) The AC-HAADF-STEM image for high-order Ru ACs in 0.5*R*/300H. The reaction conditions were as follows: 5 g of plastic, 0.5 g of catalyst, 280 °C, 24 h, 300 rpm, in a 50 mL stainless steel reactor, with 2.0 MPa of Ar.

He serving as the carrier gas. The average linear velocity was set to 21.791 cm/s. The GC oven was initially held at 35 °C for 5 min, followed by a temperature ramp of 5 °C/min to 100 °C, with a final hold at 100 °C for 25 min. Data interpretation was performed using Qualitative Analysis 12.0 by comparing it to serial standard gas.

Gaseous H_2 was introduced into the GC−MS system using valve injection (0.25 mL of quantitative ring) at a split ratio of 10:1. Hydrocarbons were resolved using an HP-AL/S capillary column (length: 30 m; diameter: 0.25 mm; film thickness: 5 μm; Agilent), with high-purity N_2 serving as the carrier gas. The average linear velocity was set to 25.373 cm/s. The GC oven was initially held at 60 °C for 5 min. Data interpretation was performed using Qualitative Analysis 12.0 by comparing to standard gas.

Liquid products were quantitatively determined by gas chromatography−mass spectrometry (GC−MS) using an HP-PONA capillary column with an MS detector (5977C GC/MSD, Agilent, He carrier gas). *n*-Hexadecane, 1-octene, cyclohexane, cyclopentene, benzene, o-xylene, mesitylene, and naphthalene were used as external standard substances.

The detailed procedures can be listed as follows:

Samples (1 μL) were introduced into the GC−MS system using an automatic liquid sampler with a split ratio of 5:1. Hydrocarbons were resolved using an HP-PONA capillary column (length: 50 m; diameter: 0.20 mm; film thickness: 0.50 μm; Agilent), with high-purity He serving as the carrier gas. The average linear velocity was set to 25.122 cm/s. The GC oven was initially held at 40 °C for 5 min, followed by a temperature ramp of 5 °C/min to 300 °C, with a final

https://doi.org/10.1021/acscatal.5c06674
ACS Catal. 2026, 16, 2194−2208

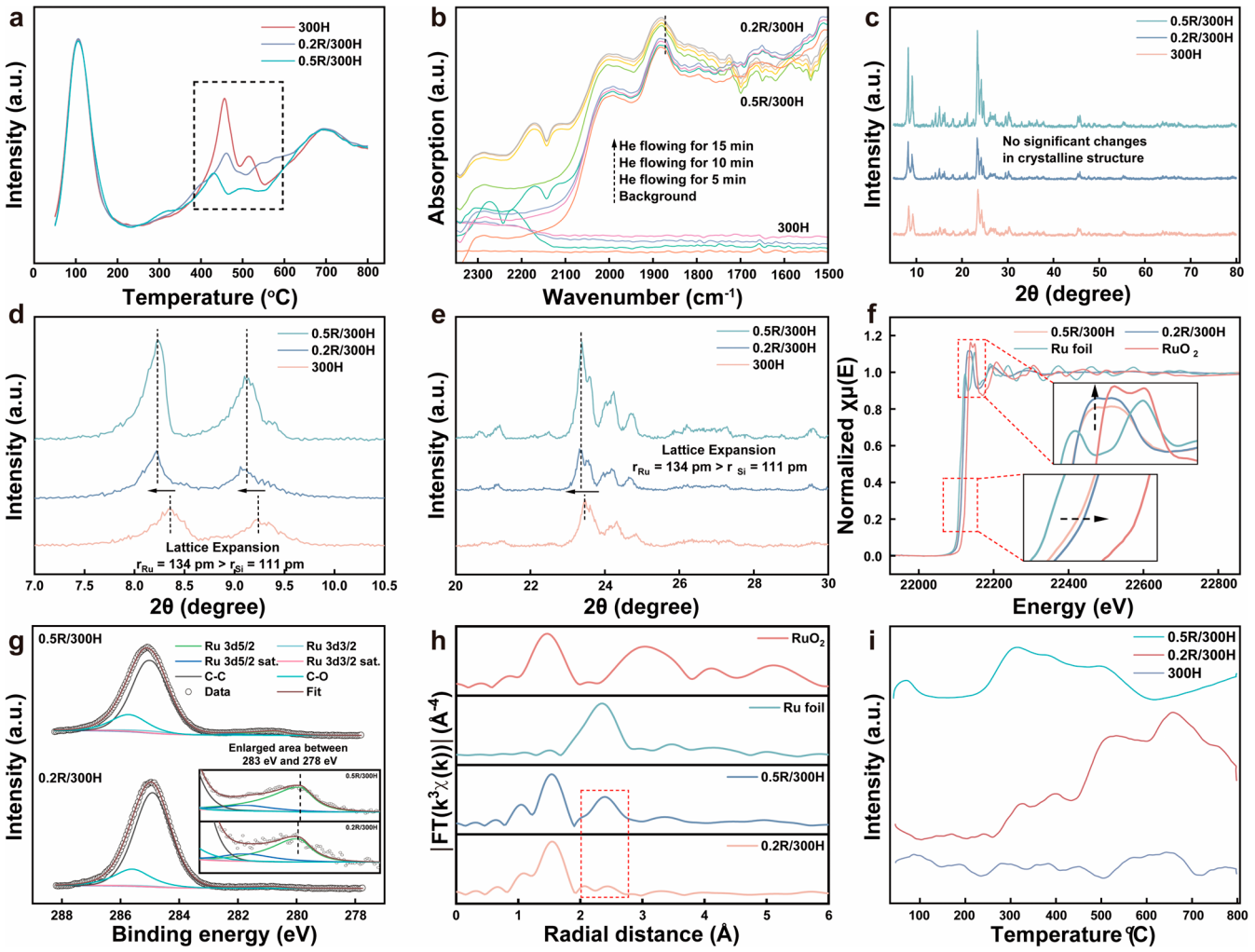

Figure 2. Structural and electronic properties of 300H, 0.2*R*/300H, and 0.5*R*/300H. (a) NH_3-TPD analysis. (b) CO-DRIFTS spectra within 2250−1500 cm^{-1} by flowing He gas at different times. C denotes cyclohexane. (c) XRD spectra. (d) XRD spectra, showing the enlarged area between 7° and 10.5°. (e) XRD spectra, showing the enlarged area between 20° and 30°. (f) Ru−K edge XANES spectra. (g) Ru 3d XPS spectra. (h) EXAFS spectra. (i) H_2-TPR analysis.

hold at 300 °C for 3 min. The ion source and quadrupole temperatures were maintained at 230 and 150 °C, respectively. Mass spectrometry was conducted in full scan mode, with a scan range of m/z = 40−800. Data interpretation was performed using the National Institute of Standards and Technology (NIST23) mass spectral library within an unknown substance analysis (Quant-My-Way, MassHunter Workstation, version 12.1).

The selectivity for the hydrocarbon C_nH_m was determined based on the C atom content and calculated according to the following formula:[13]

$$\text{Selectivity for } C_nH_m = \frac{nC_nH_m}{\sum_i iC_iH_m} \times 100\%$$

where C_nH_m denotes the moles of individual hydrocarbon product, n represents the number of C atoms in C_nH_m, and i indicates the positive integer starting from 1.

The conversion was calculated based on the following formula:[13]

$$\text{conversion } (\%) = \left(1 - \frac{m_{\text{solid hydrocarbons}}}{m_{\text{added plastics}}}\right)$$

The turnover frequencies (TOFs) were calculated based on the following formula:[13]

$$\text{average mass activity} = \frac{m_{plastics} - m_{solid\ hydrocarbons}}{m_{added\ metal\ mass} \times t_{reaction\ time}}$$

Density Functional Theory (DFT) Simulation

Spin-polarized first-principles calculations were performed by the DFT using the Vienna Ab initio Simulation Package (VASP).[14] The generalized gradient approximation (GGA) with the Perdew−Burke−Ernzerhof (PBE) functional was used to describe the electronic exchange and correlation effects.[15−17] Uniform G-centered *k*-point meshes with a resolution of 2π *x* 0.05 $Å^{-1}$ and Methfessel−Paxton electronic smearing were adopted for the integration in the Brillouin zone for geometric optimization. The simulation was run with a cutoff energy of 500 eV throughout the computations. The geometry optimization was considered convergent when the electronic energy and Hellmann−Feynman forces convergence criterion were smaller than 10^{-5} eV and 0.03 eV $Å^{-1}$, respectively. In the calculation, Grimme's DFT-D3 methodology was used to describe the dispersion interactions.[18] The dehydrogenation energy barrier was estimated using the Nudged Elastic Band (NEB) method.[19]

The adsorption energy of C_6H_{14}, C_6H_{12}, and C_6H_6 onRu_{10}@HZSM-5 and Ru[101] surfaces was calculated by the following equation:

$$\Delta G(\text{ads}) = G(\text{surface} + \text{mol})G(\text{surface})G(\text{mol})$$

where *G* (surface + mol), *G* (surface), and *G* (mol) represent the energy of C_6H_{14}, C_6H_{12}, and C_6H_6 adsorbed on Ru_{10}@HZSM-5 and

https://doi.org/10.1021/acscatal.5c06674
ACS Catal. 2026, 16, 2194−2208

Ru [101] surfaces, energy of Ru_{10}@HZSM-5 and Ru (101) surfaces, and energy of C_6H_{14}, C_6H_{12}, and C_6H_6 molecules, respectively.

Note that the rationality over DFT model selection is supplemented in Supporting Information (section: DFT Simulation: The rationality over DFT model selection).

The other detailed materials and methods are elaborated in Supporting Information.

RESULTS AND DISCUSSION

Unraveling the Relationship between Upcycling Performance and Active Site Properties

To examine the structure sensitivity of Ru in hydrogen- and solvent-free thermal polymer upcycling reactions, a series of Ru-loaded HZSM-5 catalysts with varying metal loadings were constructed (i.e., impregnation and reductive calcination methods, Figure S1) and investigated for their catalytic performance in plastic upcycling (Figures S2, S3, and 1a−d). The 0.5*R*/300H catalyst exhibited the highest low-density polyethylene (LDPE) conversion of 62.93% and aromatic selectivity of 70.43%, surpassing all other loading configurations, with corresponding conversion/selectivity values for the 300H, 0.2*R*/300H, 0.35*R*/300H, 0.75*R*/300H, 1*R*/300H, 2*R*/300H, and 3*R*/300H catalysts being 35.52/29.13%, 41.61/48.43%, 47.88/49.87%, 53.54/59.94%, 51.66/43.65%, 49.41/48.07%, and 50.37/51.10%, respectively. These findings underscored the superior performance of medium-loading Ru compared to low-loading Ru catalysts. Supplementary analysis of low (0.2 wt %), medium (0.5 wt %), and high loading (2 wt %) samples is provided in the section "Loading-activity analysis" in Supporting Information. The nuclear magnetic resonance (NMR) spectroscopy analysis of the liquid products revealed consistent results, showing a higher proportion of aromatics-related H in the 0.5*R*/300H/LDPE system (H_{Ar+Ph}/H_{Total} = 0.5) compared to the 0.2*R*/300H/LDPE system (H_{Ar+Ph}/H_{Total} = 0.1) (Figure 1f,g). In addition, it can be concluded that the Ru species may preferentially substitute the Brønsted acid sites (BASs), thereby preventing side reactions such as β-scission-facilitated C−C cleavage while intrinsically enabling synergistic interactions with BASs. This was supported by the observed lower conversion and aromatics selectivity over pure HZSM-5-300H.[20]

The upcycling capacity of various common supports (Hβ, HZSM-5-75H, and HZSM-5-150H) and metal (Ir) was evaluated (Figure 1e). Ru species supported on Hβ-zeolite, Ir species supported on HZSM-5-300H, Ru species supported on HZSM-5-150H, and Ru species supported on HZSM-5-75H all demonstrated a metal-loading dependency, with higher loadings showing improved upcycling activity and aromatic selectivity compared to lower loadings. This finding underscores the broader applicability of this trend across different support materials. For model simplification, HZSM-5-300H and Ru species were selected as representative support and active sites, with loading amounts of 0.2 and 0.5 wt % chosen for metal incorporation.

Note that the relationship between the yields of partial products—namely, alkanes, alkenes, cycloalkanes, cycloolefins, and aromatics—and metal loading was meticulously examined. It was evident that low Ru loading in 300H catalysts substantially promoted alkane/alkene formation when compared to the 0.5*R*/300H catalyst (Figure S2d). This enhancement was ascribed to the increased presence of moderate acid sites (which facilitate β-scission) in the 0.2*R*/300H catalyst, in contrast to that of the 0.5*R*/300H catalyst (Figure 2a). These factors synergistically facilitated more efficient C−C cleavage, thereby augmenting alkane/alkene yields. BASs play a critical role in the conversion of C═C bonds into carbenium ions but do not mediate the dehydrogenation of polymer chains to form additional C═C bonds. When an excess of C═C bonds is converted into carbenium ions without a corresponding increase in C═C bonds, a deficiency in available C═C bonds for interaction with carbenium ions occurs. This imbalance leads to a pronounced tendency for β-scission rather than cyclization.[13,21] Consequently, the 0.5*R*/300H catalyst exhibited superior performance in both dehydrogenation (by optimizing the C═C to carbenium ion ratio through metal−acid balance, thereby favoring cyclization and inhibiting β-scission) and aromatization (via efficient dehydro-aromatization, significantly enhancing aromatics formation). This was evidenced by its minimal alkane/alkene yields and maximal production of cyclohexane, cycloolefins, and aromatics. In summary, the product distribution analysis highlighted the enhanced dehydro-aromatization capacity of the 0.5*R*/300H catalyst, while the 0.2*R*/300H catalyst demonstrated a superior β-scission capacity. It is noteworthy that the hydrogenolysis contribution of the 0.2*R*/300H catalyst can be considered negligible owing to its weak H_2 binding capacity (Figure 2i)

The influence of metal loading on the yields of partial products, such as alkanes, alkenes, cycloalkanes, cycloolefins, and aromatics, was studied in depth. It was found that a lower Ru loading in the 300H catalyst led to a higher production of alkanes and alkenes compared to the 0.5*R*/300H catalyst (Figure S2d). This effect was attributed to a greater presence of moderate acid sites in the 0.2*R*/300H catalyst, which facilitated β-scission, unlike in the 0.5*R*/300H catalyst (Figure 2a). These acid sites promoted more efficient C−C bond cleavage, resulting in higher alkane/alkene yields. BAS is essential for converting C═C bonds into carbenium ions but does not facilitate the dehydrogenation of polymer chains to form additional C═C bonds. When an excess of C═C bonds is converted into carbenium ions without a corresponding increase in available C═C bonds, the imbalance leads to a preference for β-scission over cyclization.[13,21] As a result, the 0.5*R*/300H catalyst showed better performance in dehydrogenation and aromatization, achieving high yields of cyclohexane, cycloolefins, and aromatics while minimizing alkanes and alkenes. In summary, the 0.5*R*/300H catalyst demonstrated an appropriate dehydro-aromatization ability, whereas the 0.2*R*/300H catalyst showed a higher tendency for β-scission. The hydrogenolysis contribution from the 0.2*R*/300H catalyst was minimal due to its weaker H_2 binding ability (Figure 2i).

Note that the techno-economic analysis (TEA) revealed that the 0.5*R*/300H configuration demonstrated a markedly superior economic performance relative to the 2*R*/300H counterpart (Table SE1−8 and Figure SE1). Specifically, the ROI, PBP, IRR, and NPV for the 0.5*R*/300H configuration were 30.06%, 2.66 years, 16%, and \$1,778,301.25, respectively, without depreciation. In stark contrast, the 2*R*/300H configuration failed to demonstrate economic viability, as indicated by a negative annual gross profit of -\$2453851.7, without depreciation, primarily due to disproportionate production costs exceeding annual sales revenue. This adverse economic outcome was chiefly due to the combination of a relatively low product yield and the high cost associated with incorporating noble Ru. Consequently, it can be conclusively inferred that the incorporation of ACs into HZSM-5 catalysts

https://doi.org/10.1021/acscatal.5c06674
ACS Catal. 2026, 16, 2194−2208

offered significantly greater economic feasibility compared to that of the incorporation of NPs.

Exploring the Structural and Electronic Characteristics of Active Sites

Subsequently, aberration-corrected high-angle annular dark field-scanning transmission electron microscopy (AC-HAADF-STEM) was employed to establish a correlation between the atomic structural characteristics and the upcycling performance (Figure 1h(i)). The 0.5*R*/300H sample predominantly displayed aggregates of isolated Ru atoms, with no intact crystal facets identified. As the Ru loading was reduced from 0.5 wt % to 0.2 wt %, the distinct atomic ensembles disappeared, and the geometry of the Ru ACs transitioned from loosely bound ensembles of SAs to fully isolated atomic sites, approaching the characteristics of single-atom catalysts (SACs). However, neither linearly adsorbed CO nor bridged-bond CO signals were observed for 0.2*R*/300H, highlighting its unique intermediate state between SAs and ACs (Figure 2b). Therefore, the Ru species in 0.2*R*/300H and 0.5*R*/300H were defined as low-order Ru ACs and high-order Ru ACs, respectively. Therefore, it can be inferred that high-order ACs with an appropriate assembly degree facilitate polymer upcycling reactions more efficiently than low-order ACs with excessively isolated SAs. In a similar vein, theoretical studies have demonstrated that the adsorption of dodecahydro-*N*-ethylcarbazole (DNEC) necessitated the presence of multiple metal sites.[22] In this regard, fully exposed Pd ACs with an average Pd−Pd coordination number of 4.4 preferentially facilitate both the activation of reactants and the desorption of products, whereas Pd SAs exhibited minimal activity.[23] Indeed, in numerous cases, ACs, NPs, or even extended domains of surface facets featuring continuous metal sites—existing in a metallic state rather than the cationic state typical of isolated metal SAs—are essential for the dissociation and/or formation of the target chemical bonds.[23,24] Note that the definition of NPs and ACs in this study was supplemented in the section "The definition of NPs and ACs in this study" in Supporting Information.

In a separate study, the 0.5*R*/300H and 2*R*/300H catalysts were chosen to explore the differences in upcycling behaviors between ACs and NPs. This investigation systematically examined the catalytic mechanisms associated with highly isolated atomic sites (0.2 wt %) and ACs (0.5 wt %) with discrete atomic sites, providing a detailed comparison of their respective roles and efficiencies. These findings confirmed that Ru SAs and Ru AC-supported 300H preferentially promote β-scission and dehydrogenation/aromatization, respectively. Subsequently, the structural and electronic properties of Ru SAs and Ru AC-supported 300H were further examined in greater detail through a variety of characterization techniques.

The characteristics of acidic sites and pore structures were initially investigated. NH_3-temperature-programmed desorption was employed to examine the acidity profiles, revealing enhanced medium-strong acidity sites between 400 and 600 °C for 0.2*R*/300H compared to 0.5*R*/300H (Figure 2a). This suggested that the superior upcycling capacity of 0.5*R*/300H could be attributed more to its optimal metal structure. In contrast, pyridine-Fourier transform infrared spectroscopy (FTIR) analysis revealed a weaker acid intensity for 0.2*R*/300H relative to 0.5*R*/300H (Figure S8). These discrepancies can be ascribed to the differing interactions between NH_3 and pyridine molecules, with NH_3 more readily penetrating and interacting with HZSM-5 than with pyridine. Ru incorporation significantly affected the densities and intensities of BASs and Lewis acid sites (LAS), primarily due to its strong interaction with HZSM-5 or its role as an intrinsic acid center, which occurred via a reductive solid-state ion-exchange process.[20] The absorption bands observed at 3735 and 3591 cm^{-1} in DRIFTS are typically attributed to the external silanol groups (Si−OH) and the bridge OH groups linked to BASs, respectively (Figure S9). The nearly complete absence of these bands in the samples 0.2*R*/300H and 0.5*R*/300H indicated that Ru was substituted by BASs during the reduction process at 450 °C (reductive solid-state ion-exchange mechanism).[20] The correlation between LDPE upcycling and mass transport was excluded due to the nearly identical pore characteristics (Figure S10 and Table S3). Furthermore, enhanced coke deposition was observed for the 0.2*R*/300H compared to 0.5*R*/300H, as evidenced by the greater mass loss between 380 and 650 °C.[25] This can be attributed to the inferior metal−acid balance, which facilitated prolonged intermediate retention and consequently promoted coke formation.

Subsequently, the structural and electronic properties of 300H, 0.2*R*/300H, and 0.5*R*/300H were systematically investigated. X-ray diffraction (XRD) was initially employed to examine the crystal structures (Figure 2c−e). No sharp diffraction peaks corresponding to Ru species (i.e., 2 θ = 44.005°, indexed to the (1 0 1) lattice plane, PDF#06-0663) were observed, indicating that the Ru species were highly dispersed within the zeolite framework. Notably, significant negative peak shifts were observed for 0.2*R*/300H and 0.5*R*/300H compared with 300H, suggesting lattice expansion. The observed variations in lattice parameters can be attributed to the stress enhancement induced by the interactions between the metal and the support. For instance, lattice insertion during metal−support interaction was confirmed between Ir ACs and WO_3 (i.e., Ir ACs atomically embedded into the lattice of WO_3 support).[26]

X-ray absorption spectroscopy (XAS) was employed to investigate the chemical state changes responsible for the differences in upcycling capacities (Figure 1). Initially, the electronic state of the Ru species was probed by X-ray absorption near-edge structure (XANES), which revealed the distribution of normalized white-line intensity and edge energy for 0.2*R*/300H and 0.5*R*/300H, lying between those of Ru foil and RuO_2. This indicated the presence of a cationic Ru (Figure 2f). As the Ru loading decreased from 0.5 to 0.2 wt %, both the white-line intensity and edge energy progressively increased, suggesting an increase in the cationic state of Ru with enhanced atomic dispersion. These findings were further supported by X-ray photoelectron spectroscopy (XPS) analysis (Figures 2g and S11), which showed shifts in the binding energies of Ru 3d5/2 and Ru 3d3/2 from 280.77 and 284.97 eV 2 for 0.2*R*/300H to 280.71 and 284.91 eV for 0.5*R*/300H, respectively (Figure 2g), highlighting the close relationship between the Ru valence state and atomic assembly. Electron loss was observed for Si and O species, evidenced by the peak shifts from 103.9 to 103.95 eV (for Si species) and from 533.25 to 533.35 eV (for O species) for 0.2*R*/300H and 0.5*R*/300H, respectively, indicating the electron exchange between Ru species and HZSM-5 support (Figure S11b,c). Similarly, an increased electron loss was detected for Al species in 0.2*R*/300H compared to 0.5*R*/300H and 300H, indicating electron exchange between the Ru species and the acid sites (Figure

https://doi.org/10.1021/acscatal.5c06674
ACS Catal. 2026, 16, 2194−2208

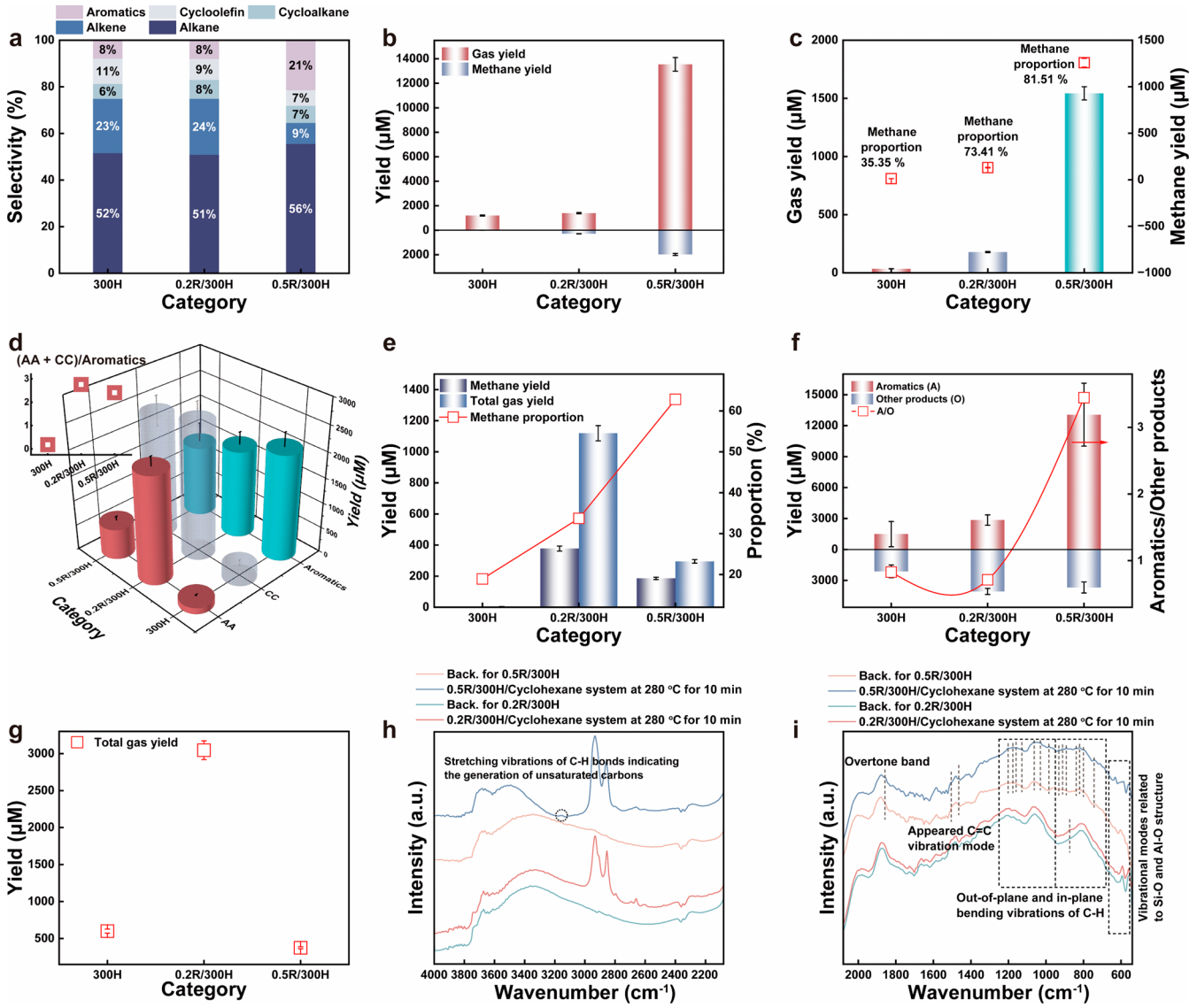

Figure 3. A comprehensive investigation of mechanisms in polymer upcycling through probing reaction. (a) Selectivity analysis for alkane, alkene, cycloalkane, cycloolefin, and aromatic products in catalysts/n-hexadecane/H_2-free/solvent-free systems. (b) The yields of gas and methane products in catalysts/n-hexadecane/H_2/solvent-free systems. (c) The yields of gas and methane products as well as methane proportion in catalysts/cyclohexane/H_2/solvent-free systems. (d) Yield determination of alkane + alkene (AA) and cycloalkane + cycloalkene (CC) and the AA + CC to aromatics ratio in catalysts/benzene/H_2/solvent-free systems. (e) The yields of gas and methane products as well as methane proportion in catalysts/benzene/H_2/solvent-free systems. (f) The yields of aromatics and other products with the aromatics-to-other products ratio in catalysts/cyclohexane/H_2-free/solvent-free systems. (g) The yield of gas product in catalysts/cyclohexane/H_2-free/solvent-free systems. (h) In situ DRIFTS analysis of 0.2*R*/300H/cyclohexane/H_2-free/solvent-free and 0.5*R*/300H/cyclohexane/H_2-free/solvent-free systems (g) from 4000 to 2080 cm^{-1} and (i) from 2080 to 540 cm^{-1}. High-resolution figures can be viewed in Figures S20 and S21.

S11d). In addition, the most positive peak position of Al 2p in 0.2*R*/300H verified its strong BAS acidity due to enhanced H^+ adsorption capacity (Figure 2a). These results underscored the strong correlation between the atomic structural characteristics and their electronic properties, likely due to variations in atomic interaction forces (Figure 1h(i)) and the intensity of metal−support interactions.

The EXAFS results revealed that both 0.2*R*/300H and 0.5*R*/300H displayed Ru−O scattering at approximately 2.02 and 2.01 Å, respectively. However, as Ru loading decreased, the Ru−Ru scattering weakened, and the coordination number of Ru−Ru (N(Ru−Ru)) diminished from 0.76 ± 0.36 to undetectable levels, indicating the loss of well-defined Ru ACs with decreasing atomic loading (Figures 2h andS12−14 and Table S4). These findings highlighted significant structural transformations in the Ru species, shifting from well-defined Ru ACs (high-order Ru ACs) in 0.5*R*/300H to highly isolated Ru SAs (low-order Ru ACs), which likely account for the observed abrupt changes in polymer upcycling efficiency (Figures 1a−e and S3). Notably, the Ru K-edge EXAFS features of the reduced samples may completely disappear if the incorporated Ru exists at an extra-framework position.[20] The distinct EXAFS characteristics further underscored the strong interaction (i.e., robust coordination) between the Ru species and the HZSM-5 framework.

The H_2-TPR technique was employed to assess the hydrogen binding capacity (Figure 2i). It was observed that 0.5*R*/300H exhibited a more pronounced continuous

https://doi.org/10.1021/acscatal.5c06674
ACS Catal. 2026, 16, 2194−2208

absorption band in the low-temperature region for H_2 compared with 0.2*R*/300H, which showed its absorption band in the higher-temperature range. This suggested a greater H_2 binding capacity for Ru ACs with more step sites, in contrast to that of 0.2*R*/300H, which predominantly featured isolated atomic sites. Furthermore, Ru ACs are expected to exhibit superior H_2 spillover capacity (Chen et al., 2022). To sum up, at a reaction temperature of 280 °C, the hydrogen utilization capacity followed the order 0.5*R*/300H > 0.2*R*/300H > 300H. Consequently, the relationship between the morphologies of Ru assemblies and their polymer upcycling performance can be delineated, as further elucidated through targeted probe experiments.

A Comprehensive Examination of the Mechanisms Underpinning Polymer Upcycling through Probing Reaction

Plastic thermal recycling involves a complex interplay of reactions, including β-scission, hydrogenolysis, dehydrogenation, aromatization, and hydrogenation, each of which is explored in detail in the following section. Hexadecane was employed as a substrate to evaluate the system's efficiency in converting medium-chain alkanes (Figures 3a and S15). The results revealed a significant reduction in aromatic selectivity, which dropped from 70% to 21% in the 0.5*R*/300H group (Figure 1a−d), thereby supporting the rationale for utilizing polymers as reactants to preferentially generate aromatics. Furthermore, these findings indicate that long-chain alkanes are the primary contributors to the aromatization process, as the upcycling of hexadecane was predominantly driven by the cleavage pathway rather than the aromatization pathway. This is substantiated by the higher selectivity for alkanes and alkenes compared to other products. Additionally, high-order Ru ACs demonstrated superior aromatization and conversion capacities relative to low-order Ru ACs, even when using medium-chain alkane reactants. This was reflected in a higher aromatics selectivity (21% vs 8% for 0.5*R*/300H and 0.2*R*/300H, respectively) and overall yield s81,473.05 μM vs 57371.64338 μM for 0.5*R*/300H and 0.2*R*/300H, respectively). The hexadecane upcycling results further corroborated the enhanced efficiency/selectivity of 0.5*R*/300H in alkane transformation and aromatization compared to 0.2*R*/300H.

Hexadecane, a medium-chain hydrocarbon, was chosen as the model substrate to evaluate the hydrogenolysis capacity of the 0.2*R*/300H and 0.5*R*/300H catalysts. In the 0.5*R*/300H/hexadecane/H_2 system, a higher yield of short-chain gaseous hydrocarbons (C1−C6) was produced (13544.46145 μM) compared to the 0.2*R*/300H/hexadecane/H_2 system (1391.85383, Figure 3b), along with increased H_2 consumption (7923.70235 μM vs 25532.06319 μM for 0.2*R*/300H and 0.5*R*/300H, respectively, Figure S16). This suggested that higher-order Ru ACs may energetically favor hydrogenolysis-mediated C−C cleavage over low-order Ru ACs, as more well-defined crystallographic facets are generally more efficient in alkane adsorption (Chen et al., 2022a). Additionally, the 0.5*R*/300H/hexadecane/H_2 system generated a higher volume of liquid hydrocarbons (dominated by alkane) than the 0.2*R*/300H/hexadecane/H_2 system (12257.36 μM vs 33565.05 μM for 0.2*R*/300H and 0.5*R*/300H, respectively, Table S5). This further indicated that 0.5*R*/300H had superior H_2 utilization efficiency for both C−C cleavage (hydrogenolysis) and recombination (metal−acid synergism) compared to 0.2*R*/300H. However, a greater amount of short-chain hydrocarbons was produced in the 0.2*R*/300H system compared to 0.5*R*/300H during LDPE upcycling (Figure 1a−d), emphasizing that the suboptimal metal−acid balance led to excessive C−C cleavage (β-scission) rather than hydrogenolysis-supported C−C scission. In summary, the weak hydrogenolysis activity of 0.2*R*/300H can be attributed to the limited H* release induced by weak dehydroaromatization (Figure 3f) and unfavorable interactions with reactants and H* (Figure 2i). Notably, chain extension products (carbon numbers greater than 16) were observed in both systems (dominated by alkane), attributed to the synergy between Ru metal (cleaving larger hydrocarbons into smaller fragments) and acidic sites (enabling chain extension via recombination and rearrangement). Moreover, similar results were observed in the hydrogenolysis of cyclohexane, where a higher yield of gaseous products and an increased proportion of methane (i.e., high and low Ru loadings favor terminal C−C cleavage and internal C−C cleavage, respectively) were detected for 0.5*R*/300H compared to 0.2*R*/300H (1543.44416/1258.10555 μM vs 178.4063/130.96808 μM, Figures 3c and S17).[27] These findings suggest that 0.5*R*/300H, compared to 0.2*R*/300H, can preserve the yield of aromatics by inhibiting the β-scission reaction rather than hydrogenolysis during the polymer upcycling process. From another perspective, appropriate hydrogenolysis can more readily depolymerize the polymer for subsequent transformation. Specifically, this enhanced H* utilization contributed to the reduction of coke formation (similar results can be concluded for Ru-loaded 150H and 75H samples, Figures S18 and S31a,b) and the inhibition of excessive β-scission. The reduction in coke formation can be attributed to the hydrogenation of organic molecules, the suppression of polymerization reactions, and the modulation of cracking pathways, all of which effectively prevented the generation of larger molecular species that are prone to coke deposition.[28] The suppression of β-scission was achieved through the supply of C═C via H*-promoted C−H bond activation, which in turn facilitated the cyclization reaction.[13]

Rehydrogenation of the benzene ring can significantly reduce the yield of aromatics. For instance, in the Pt(111) single crystal-mediated cyclohexane dehydrogenation reaction, concurrent cyclohexane dehydrogenation and benzene hydrogenation were observed by switching temperatures.[29] Thus, the rehydrogenation capacity was evaluated over 0.2*R*/300H and 0.5*R*/300H systems using the benzene ring as a probe molecule. More hydrogenation products of the benzene ring (e.g., cyclohexane + cycloalkene (C/C)-related products) and hydrogenolysis/β-scission products (e.g., alkane + alkene (A/A)-related products) were observed in the 0.2*R*/300H/benzene/H_2 system (2120.06402 μM for AA and 2593.86385 μM for CC, Figure 3d) compared to the 0.5*R*/300H/benzene/H_2 system (610.11389 μM for AA and 2372.41766 μM for CC, Figure 3d). In addition, more H_2 consumption was observed in the 0.5*R*/300H system compared to the 0.2*R*/300H (19201.9957 μM vs 13487.19305 μM, Figure S19). Specifically, more alkanes and alkenes were observed in the benzene hydrogenation reaction mediated by 0.2*R*/300H compared with 0.5*R*/300H, suggesting that the higher number of acidic sites in 0.2*R*/300H facilitated ring hydrogenation (via acidic site-mediated destruction of π-electrons) and cracking. For example, DFT calculations confirmed that the intersection of the straight and sinusoidal channels in HZSM-5 facilitated the hydrocracking of

https://doi.org/10.1021/acscatal.5c06674
ACS Catal. 2026, 16, 2194−2208

9,10-dihydroanthracene, producing 1-benzyl-2-methylbenzene as an intermediate, with toluene, benzene, and o-xylene as the final products.[30] Similarly, it has been reported that the H_2 pulse can generate high BASs on the $PtWO_x$/C inverse catalyst, which partially aligns with the reaction conditions used in the benzene hydrogenation reaction.[31]

Furthermore, the 0.2*R*/300H/benzene/H_2 system showed a higher gas yield (377.32417 μM, Figure 3e) compared to that of the 0.5*R*/300H/benzene/H_2 system (185.37225 μM, Figure 3e). The reduced H_2 consumption for 0.2*R*/300H compared to 0.5*R*/300H further supports the conclusion that the benzene elimination was attributed to carbocation-mediated cracking (i.e., weak H_2 utilization efficiency) rather than metal AC-mediated hydrogenolysis.

In the context of benzene hydrogenation, metal clusters typically exhibit superior catalytic activity compared to BASs. This is attributed to the fact that metal clusters, particularly those composed of noble metals (e.g., platinum, palladium, and gold) or transition metals (e.g., nickel), are capable of directly dissociating hydrogen molecules into atomic hydrogen, which then facilitates the hydrogenation of the benzene ring. The metal surfaces can engage in strong interactions with the benzene ring, thereby promoting the hydrogenation process. In contrast, BASs primarily function by activating the benzene ring through protonation of its π-electron cloud, thus increasing its electrophilicity and making it more susceptible to hydrogenation. However, BAS does not provide hydrogen atoms directly but instead creates a suitable environment for the reaction. Consequently, although BASs assist in the activation of the benzene ring, their role is more indirect, rendering them less effective in driving the hydrogenation reaction compared with metal clusters, which directly participate in hydrogen dissociation and subsequent hydrogenation. Therefore, a more favorable metal−acid synergistic effect in the benzene hydrogenation reaction can be expected for 0.2*R*/300H compared to 0.5*R*/300H. These findings are supported by the enhanced production of alkyl-aromatics, which can be attributed to the initiation by both B and L acidities (632.65 μM vs 480.08 μM for 0.2*R*/300H and 0.5*R*/300H, respectively, Table S6).

The differential results between direct cyclohexane hydrogenolysis and benzene hydrogenation/hydrogenolysis suggested that the adsorbed states of cyclohexane/cyclohexene, which directly participated in further reactions (i.e., the coverage of relevant intermediates), differed from those formed upon readsorption.[32]

Cyclohexane was selected as a model substrate to compare the dehydro-aromatization capacities of 0.2*R*/300H and 0.5*R*/300H. More aromatics yields (i.e., 2846.93075 and 13064.18159 μM for 0.2*R*/300H and 0.5*R*/300H, respectively, Figure 3f) as well as larger aromatics/other products ratios (i.e., 0.7113 and 3.44665 for 0.2*R*/300H and 0.5*R*/300H, respectively, Figure 3f) were observed for 0.5*R*/300H compared to 0.2*R*/300H. Simultaneously, increased gaseous products (i.e., 3045.76845 and 374.84123 for 0.2*R*/300H and 0.5*R*/300H, respectively) were observed for 0.2*R*/300H compared to 0.5*R*/300H (Figure 3g). These results highlighted that the ring opening was more preferred over dehydrogenation in low-order Ru AC-incorporated zeolite, possibly due to its capacity of protonation in destabilizing cyclohexane with possible mechanisms of the carbonium ion mechanism and carbenium ion chain mechanism.[30,33] Superior aromatics yield, in high-order Ru ACs compared to low-order Ru ACs, which can thus be associated with the intrinsically superior dehydrogenation capacity (i.e., appropriate assembly requirement) as well as the inhibited tendency toward rehydrogenation.. The TOF for aromatics production was determined (i.e., 296.56 μM·mg^{-1} Ru·h^{-1} and 544.34 μM·mg^{-1} Ru·h^{-1} for 0.2*R*/300H and 0.5*R*/300H, respectively); the low value of 0.2*R*/300H should be attributed to the insufficient assembly of the active center. In detail, low-order Ru ACs have fewer and more isolated active sites, limiting their ability to facilitate multisite reactions that require cooperativity, compared to high-order Ru ACs.

In situ DRIFTS was utilized to further investigate the influence of particle characteristics on the dehydrogenation reaction (Figure 3h(i)). The peaks at around 2930 cm^{-1} (C−H asymmetric stretching vibration of methylene) and 2852 cm^{-1} (C−H symmetric stretching vibration of methylene) are attributed to cyclohexane adsorption. Peaks at 2319 and 2360 cm^{-1} correspond to the adsorption of CO_2, which is challenging to remove entirely. In the 0.5*R*/300H/cyclohexane system, notable C−H in-plane bending vibrations (1250−1000 cm^{-1}), C−H out-of-plane bending vibrations (910−665 cm^{-1}), C═C stretching vibrations (1600−1450 cm^{-1}), and overtone bands (2000−1650 cm^{-1}) related to substituted benzene were detected, whereas no significant signals were observed in the 0.2*R*/300H/cyclohexane system. Additionally, the C−H stretching vibrations (3300−3100 cm^{-1}) suggest the formation of unsaturated carbons (i.e., double or triple bonds), which were not clearly observed in the 0.2*R*/300H/cyclohexane system. Similarly, the peak at 3108 cm^{-1}, attributed to the ν_{CH} vibration modes of C_6H_6, was observed during 0.5 wt % Pt_n/nanodiamond@graphene (ND@G)-mediated cyclohexane dehydrogenation.[34] A 3035 cm^{-1} band corresponding to the asymmetric C−H stretching (ν(C−H)) was identified for the olefin (Cy-ene) during the investigation of the gas-phase oxidative dehydrogenation of cyclohexane over alumina-supported copper−manganese oxide catalysts.[35] Vibrations corresponding to aromatic C−H bonds (3000−3100 cm^{-1}) were observed for Pt−Ca/Al_2O_3-mediated cyclohexane dehydrogenation.[36] The bands corresponding to light olefins, such as hexene (3012, 2975, and 1645 cm^{-1}) and butene (3100, 3018, and 1645 cm^{-1}), were observed at temperatures exceeding 100 °C, 100 °C, 150 °C, and 150 °C for PdAg/Fe_2O_3, Ag/Fe_2O_3, Pd/Fe_2O_3, and Fe_2O_3, respectively, during the cyclohexane dehydrogenation reaction.[37] Vibrational modes of vinyl groups (ν(C═H)) typically appear in the range of 3100−3000 cm^{-1} during in situ DRIFTS analysis of 1-pentyne hydrogenation. The prominent band observed at 3337 cm^{-1}, corresponding to ν(H−C≡), for the Ag/Ca catalyst is attributed to the basic nature of the catalyst or its support material.[38] Aliphatic compounds, including methyl, methylene, and methine groups, are observed in the 3850−3000 cm^{-1} region of the asphaltenes.[39] These findings indicate that high-order Ru ACs are more efficient in promoting the dehydrogenation reaction compared with low-order Ru ACs, likely due to their enhanced hydrogen abstraction capability.

In summary, the superior performance of 0.5*R*/300H over 0.2*R*/300H was primarily due to its enhanced dehydrogenation capability, which effectively accelerated the initiation of depolymerization through metal−acid synergism. Furthermore, its efficient cyclization ability facilitated the formation of hexacarbon rings, while the rapid aromatization process promoted the production of aromatic compounds. At the same time, the relatively weaker rehydrogenation and balanced

https://doi.org/10.1021/acscatal.5c06674
ACS Catal. 2026, 16, 2194−2208

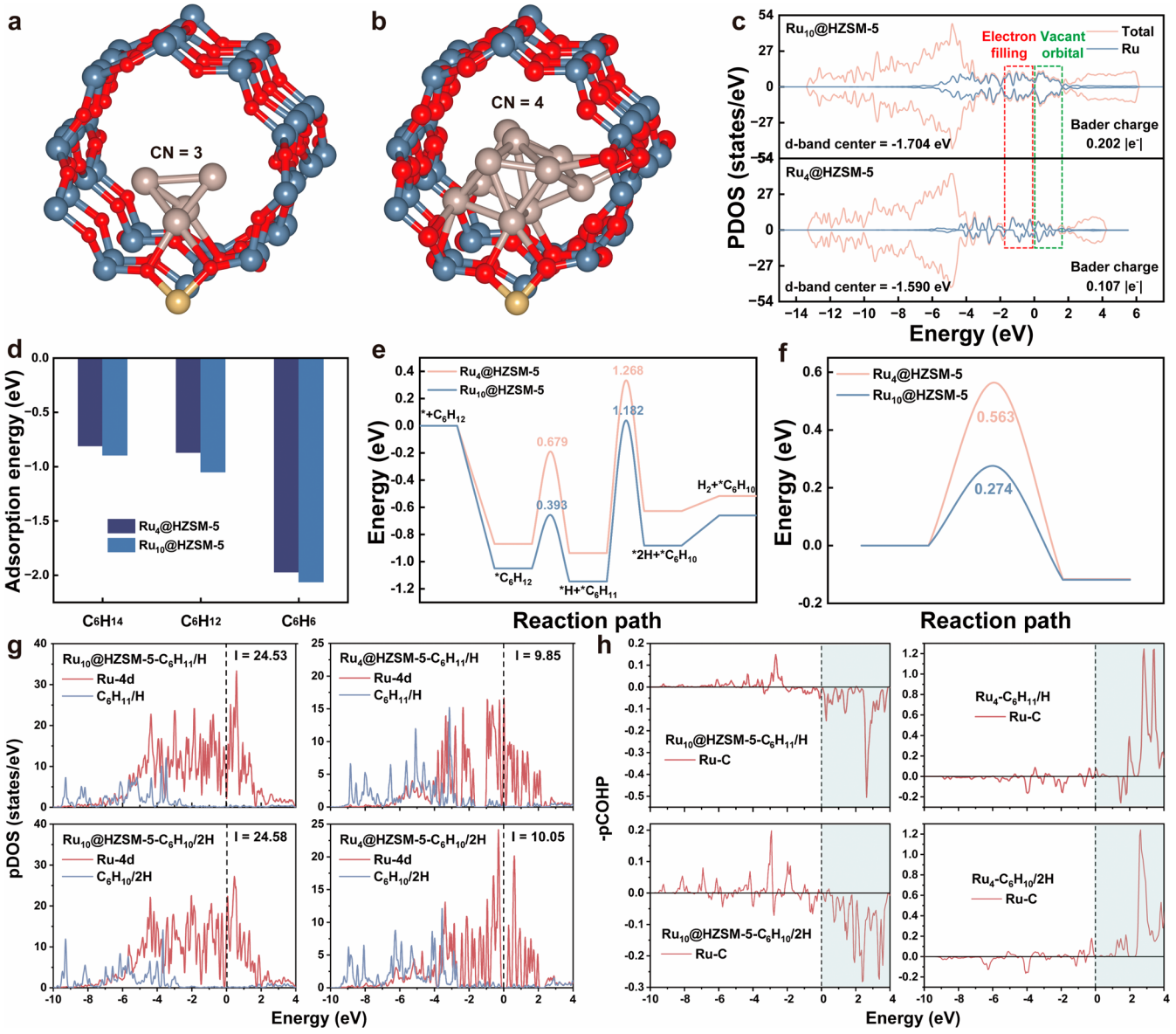

Figure 4. A comprehensive investigation of mechanisms in polymer upcycling through theoretical simulation. The optimized structures for (a) Ru_4@HZSM-5 and (b) Ru_{10}@HZSM-5. Si: cyan; Ru: gray; Al: light yellow; O: red. (c) The calculated DOS, d-band center, and Bader charge of Ru in Ru_4@HZSM-5 and Ru_{10}@HZSM-5. (d) The calculated adsorption energy of C_6H_{14}, C_6H_{12}, and C_6H_6 on Ru_4@HZSM-5 and Ru_{10}@HZSM-5. (e) Energy profiles of the step-by-step dehydrogenation from C_6H_{12} to C_6H_{10} on Ru_4@HZSM-5 and Ru_{10}@HZSM-5. (f) The calculated hydrogen migration energy barrier from H* on active sites to C_6H_{11} with C^+ on Ru_4@HZSM-5 and Ru_{10}@HZSM-5. (g) The calculated DOS of Ru_4@HZSM-5 - C_6H_{11}/H, Ru_4@HZSM-5 - C_6H_{10}/2H, Ru_{10}@HZSM-5 - C_6H_{11}/H, and Ru_{10}@HZSM-5 - C_6H_{10}/2H. I represents the integration above the Fermi level. (h) The calculated -pCOHP of Ru−C bonds in Ru_4@HZSM-5-C_6H_{11}/H, Ru_4@HZSM-5-C_6H_{10}/2H, Ru_{10}@HZSM-5-C_6H_{11}/H, and Ru_{10}@HZSM-5-C_6H_{10}/2H.

hydrogenolysis properties (appropriate H* binding capacity, Figure 2i) of 0.5*R*/300H minimized undesirable side reactions, such as aromatic hydrogenation and coke formation, while simultaneously enhancing polymer depolymerization (i.e., H*-mediated C−H activation), ultimately leading to a higher yield of aromatics.

To investigate the active site characteristics in 0.5*R*/300H during cyclohexane dehydrogenation, in situ XPS was used to track the changes in the valence states of Ru, O, and Si (Figure S22). Periodic fluctuations in the Ru 3d binding energy (280.42 eV → 280.31 eV → 280.73 eV) were observed, corresponding to similar variations in the Si 2p (103.72 eV → 103.85 eV → 103.70 eV) and the O 1s (533.15 eV → 533.22 eV → 532.98 eV) peaks. These fluctuations highlighted the metal−support interaction that drove cyclohexane dehydrogenation. The electron exchange in the Ru species underscored its key role in cyclohexane adsorption, hydrogen abstraction, and product desorption. Additionally, SixAlyO may act as an electron reservoir, storing abstracted hydrogen and enabling the sequential dehydrogenation of adsorbed aromatics, followed by the release of H_2.

A Comprehensive Investigation of the Mechanisms Involved in Polymer Upcycling through Theoretical Simulations

The theoretical models for 0.2*R*/300H and 0.5*R*/300H were carefully developed to highlight the superior properties of Ru ACs (denoted as high-order ACs with continuous active sites)

https://doi.org/10.1021/acscatal.5c06674
ACS Catal. 2026, 16, 2194−2208

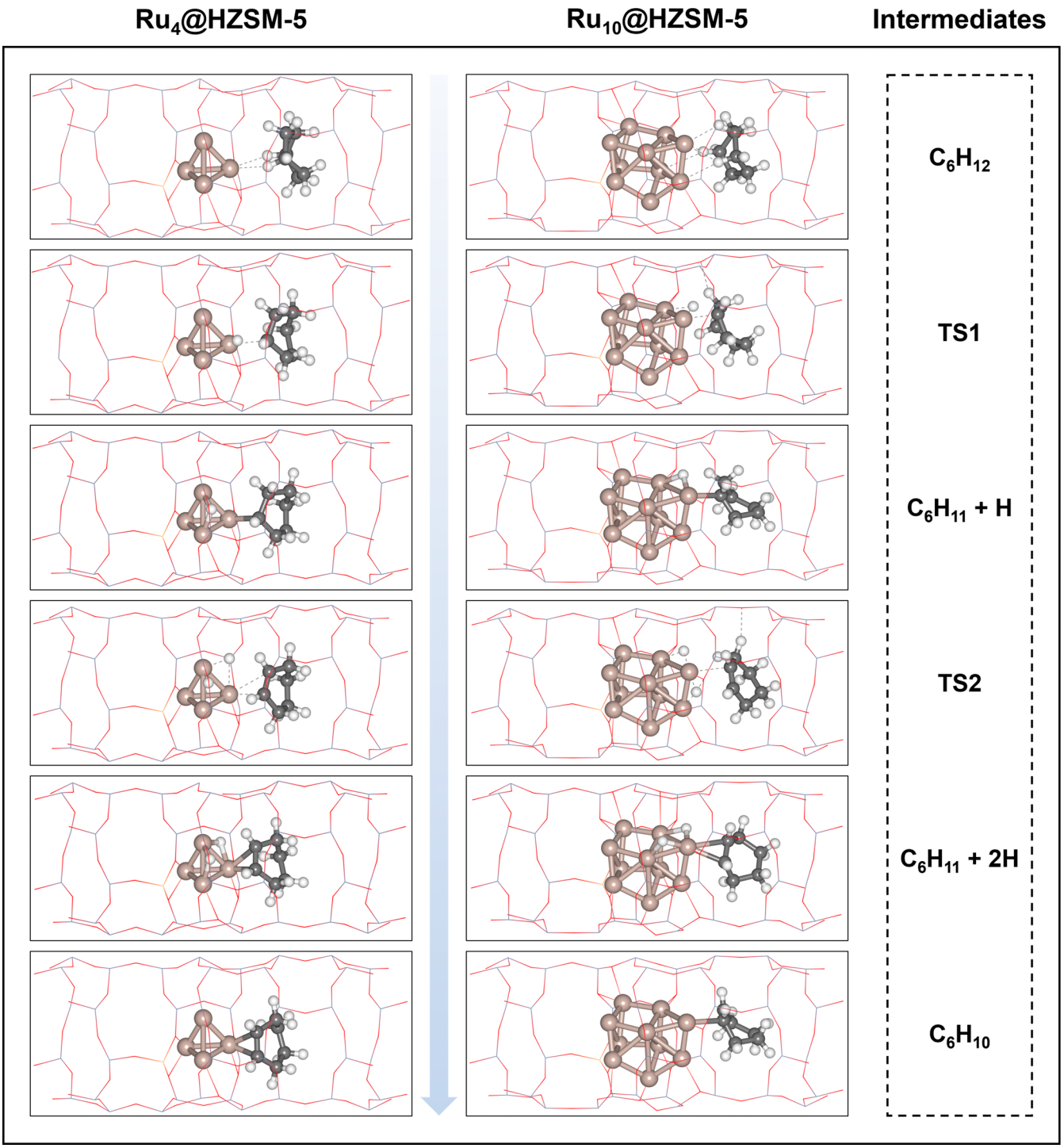

Figure 5. Optimized structures of reaction intermediates. Si: cyan; Ru: gray; Al: light yellow; O: red; C: black; H: white.

over Ru SAs (denoted as low-order ACs with isolated atomic sites) in polymer upcycling at orbital levels (Figure 4a,b). ZSM-5 was represented using the periodic MFI framework, as referenced in the Database of Zeolite Structures (http://www.iza-structure.org/databases/). Eventually, the Ru_4@HZSM-5 and Ru_{10}@HZSM-5 models were employed to represent HZSM-5-supported Ru SAs exhibiting nearly isolated atomic sites and Ru ACs with discrete Ru atoms, respectively.

The atoms located at low-order ACs and the active sites on high-order ACs exhibited average Ru−Ru coordination numbers (CNs) of 3 and 4, respectively (Figure 4a,b). As a result, their d-band centers ranged from −1.540 to −1.704 eV, with Bader charges spanning from +0.202 to +0.107 |e| (Figures 4c and S23, Tables S7 and S8). These variations had a profound effect on the binding affinities of the reactants to the active sites. According to d-band center theory,[40] it would be expected that low-order ACs exhibited a higher capacity for reactant adsorption compared to high-order ACs. However, in contrast to this prediction, the opposite trend was observed.

The adsorption energies of C_6H_{14}, C_6H_{12}, and C_6H_6 on Ru_{10}@HZSM-5 (−0.89456, −1.05012, and −1.05012 eV) were significantly higher than those on Ru_4@HZSM-5

https://doi.org/10.1021/acscatal.5c06674
ACS Catal. 2026, 16, 2194−2208

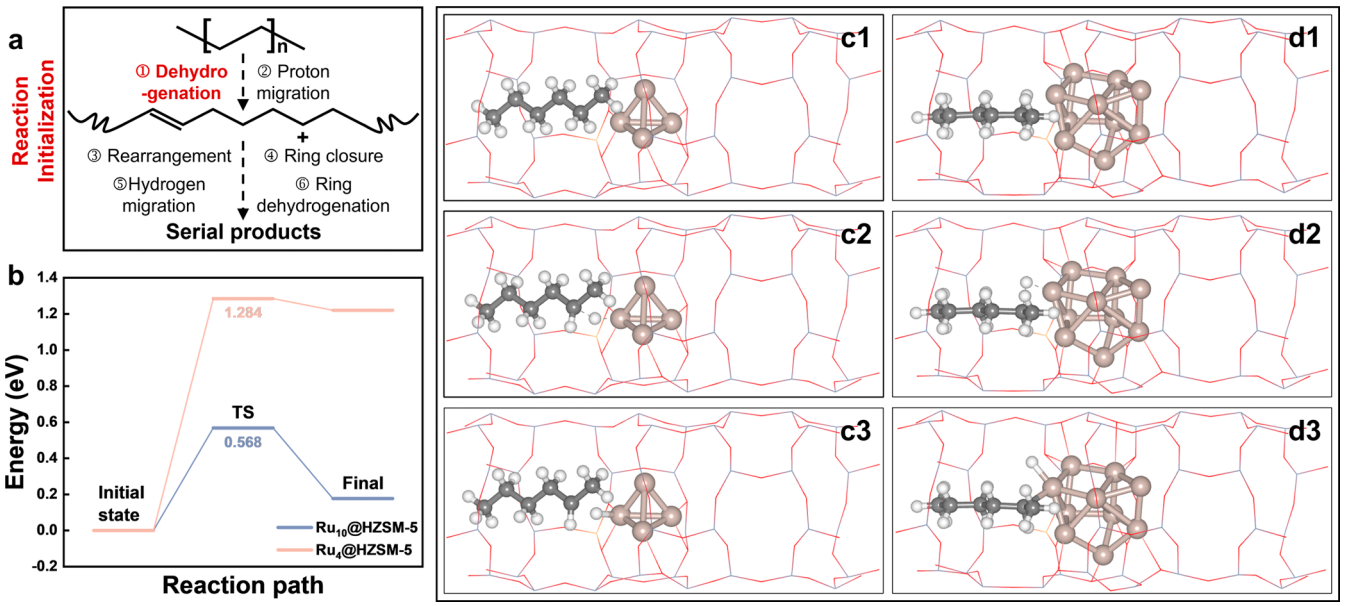

Figure 6. (a) The importance of dehydrogenation reactions in cascade reactions. (b) Energy profiles of the step-by-step dehydrogenation from C_6H_{14} to C_6H_{13} on Ru_4@HZSM-5 and Ru_{10}@HZSM-5 surfaces. (c) The reaction processes during hexane dehydrogenation on Ru_4@HZSM-5. (d) The reaction processes during hexane dehydrogenation on Ru_{10}@HZSM-5. Ru: gray; C: black; H: white.

(−0.80918, −0.80918, and −1.97158, Figure 4d and S28). The discrepancy between the d-band center and adsorption energy can be attributed to the ensemble effect for reactants (Table S8), specifically the requirement for adsorption at multiple active sites.[23] From the perspective of Bader charge analysis, Ru in the Ru_{10}@HZSM-5 surface exhibited a higher electronic density compared to Ru_4@HZSM-5 (+0.1074 vs +0.2017 eV, Figure 4c and Table S8), particularly with an enhanced electron density in the range −1 to 0 eV. This increased electronic density promoted a more effective interaction with the lowest unoccupied molecular orbital (LUMO) of C_6H_x, leading to a higher adsorption energy. Excessively strong interactions led to coke formation, whereas interactions that were too weak hindered the driving of subsequent reactions. This emphasized the crucial role of surface electronic structure characteristics in shaping the reaction process and underscored the superior ability of Ru_{10} to interact with reactants compared to Ru_4.

The core model reaction of aromatic formation (i.e., cyclohexane dehydrogenation with one H_2 molecule liberation) was investigated (Figures 4e and 5). The Ru_4@HZSM-5 surface was excessively inactive toward cyclohexane adsorption with an adsorption energy of −0.8697 eV (Figure 4e) compared to Ru_{10}@HZSM-5 with an adsorption energy of −1.05012 (Figure 4e). The weak interaction between low-order Ru ACs and C_6H_{12} hindered the subsequent dehydrogenation step, resulting in higher dehydrogenation energy barriers of 0.679 eV (first C−H activation/cleavage) and 1.268 eV (second C−H activation/cleavage), compared to 0.393 eV (first C−H activation/cleavage) and 1.182 eV (second C−H activation/cleavage) on high-order ACs. Similarly, a higher energy barrier was observed on Pd_1/G compared to Pd_{13}/G during the DNEC dehydrogenation process.[23] In catalytic processes, the strength of reactant adsorption on active sites is a critical determinant of the reaction energy barrier. When atomic sites exhibit weak adsorption toward the reactants, the interaction between the reactant and the catalyst surface becomes suboptimal, thereby inhibiting the proper activation of the reactant. This weak interaction can lead to less stable binding of the reactant, which consequently elevates the energy barrier for the subsequent reaction steps. Such a diminished adsorption strength hampers the efficient stabilization of the transition state and disrupts the favorable alignment of the reaction pathway, ultimately resulting in an increased activation energy. Hence, the existence of sufficiently strong and strategically optimized adsorption interactions at the active sites is indispensable for minimizing the energy barrier and promoting an efficient catalytic transformation.

The migration of H* to eliminate carbonium ions is a critical step in the formation of hexatomic carbon ring-containing products (i.e., dehydro-aromatization precursors). Therefore, the ability of Ru assemblies to promote hydrogen migration and stabilize or eliminate carbenium ions was assessed. Notably, a significantly higher migration energy barrier of 0.563 eV was observed for Ru_4@HZSM-5, compared to a much lower barrier of 0.274 eV for Ru_{10}@HZSM-5 (Figure 4f). These results suggested that Ru_4@HZSM-5 may not exhibit the necessary activity for efficient cyclic hydrocarbon formation, leading to slower overall reaction kinetics.

The detailed analysis of the density of states (DOS) and integrated crystal orbital Hamilton population (ICOHP) was employed to investigate the differences in catalytic activity for dehydro-aromatization between low-order and high-order Ru assemblies, with a specific focus on the intermediates C_6H_{11} + H and C_6H_{10} + 2H. On one hand, Ru_{10}@HZSM-5 exhibited a greater density of vacant orbitals (indicated by the integration above the Fermi level, Figure 4c) compared to Ru_4@HZSM-5, following the dehydrogenation of C_6H_{12} (leading to C_6H_{11} + H, Figure 4g) and C_6H_{11} (leading to C_6H_{10} + H, Figure 4g). The increased availability of empty orbitals in Ru_{10}@HZSM-5 facilitated a more favorable reaction pathway for subsequent hydrogen abstraction processes, particularly, the transfer of shared electrons from the C−H bond to the Ru−C bond. This observation is further corroborated by the more pronounced pCOHP distribution for Ru_{10}@HZSM-5 above the Fermi level

https://doi.org/10.1021/acscatal.5c06674
ACS Catal. 2026, 16, 2194−2208

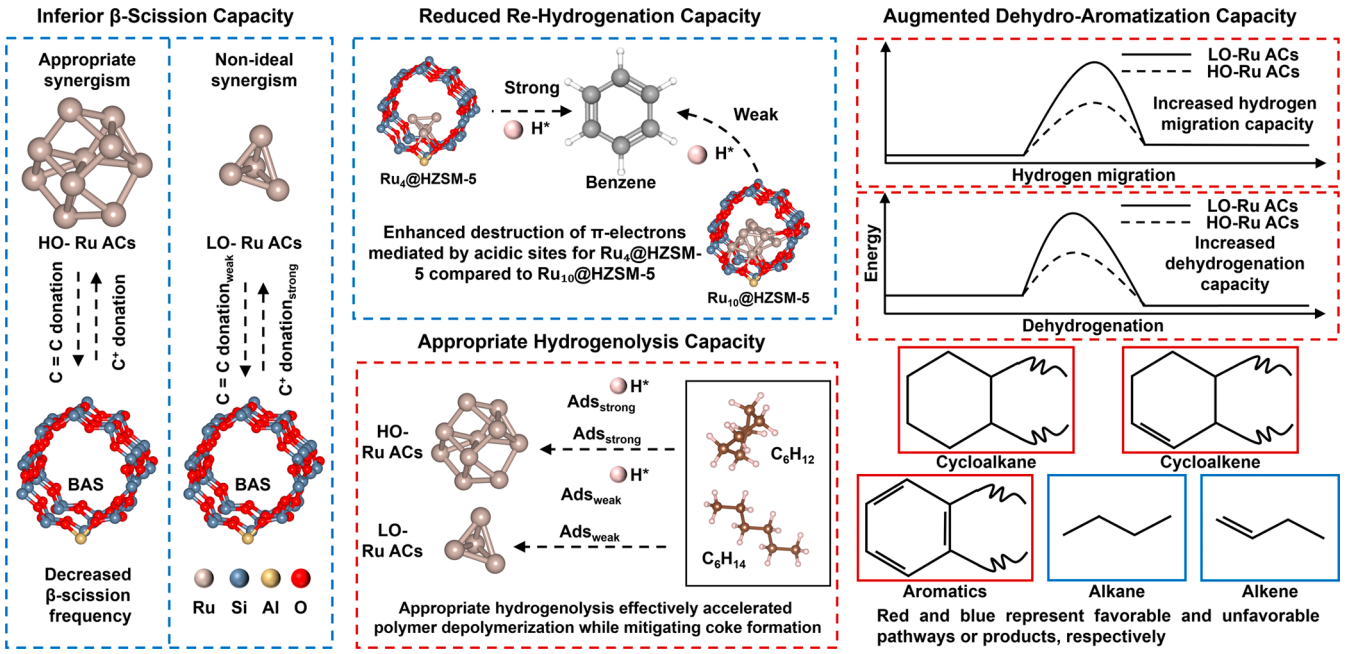

Figure 7. Proposed upcycling mechanisms for 0.2*R*/300H and 0.5*R*/300H.

(bonding characteristics), indicating stronger participation in the reaction compared to Ru_4@HZSM-5 (Figure 4h). From another perspective, the enhanced stability can be corroborated by the positive distribution of Ru−C bonding interactions, as indicated by the -pCOHP in Ru_{10}@HZSM-5, in contrast to the negative distribution observed for Ru−C bonding in Ru_4@HZSM-5 (Figure 4h). This positive distribution facilitated interaction of the active sites with hydrocarbons. More specifically, in the Ru_{10}@HZSM-5 catalyst, the negative -pCOHP value associated with the Ru−C bond suggested a stronger Ru−C bond interaction, which promoted C−H bond activation, thereby facilitating subsequent electron transfer processes. In contrast, weaker Ru−C bonding results in lower adsorption energies, which diminish the likelihood of reaction progression. Thus, the more robustly bound active sites are inherently more conducive to C−H bond cleavage and the promotion of electron transfer reactions.

Dehydrogenation reactions serve as the initiating steps in cascade reactions for plastic upgrading (Figure 6a). Specifically, the superiority of high-order Ru sites compared to low-order Ru sites in initializing polymer depolymerization can be reflected in the following aspects: ① Ru_{10}@HZSM-5 exhibited a significantly reduced dehydrogenation energy barrier during hexane dehydrogenation compared to Ru_4@HZSM-5, decreasing from 1.284 to 0.568 eV, thereby demonstrating its superior LDPE activation and dehydrogenation capacity (Figure 6b,c(1−3). ② The greater energy decline (0.0644 and 0.3913 eV for Ru_4@HZSM-5 and Ru_{10}@HZSM-5, respectively) during TS desorption further enhanced the rapid reaction cycle (i.e., adsorption−desorption circulation) during initiating the LDPE depolymerization (Figure 6b,d(1−3).

To sum up, Ru_{10}@HZSM-5 would be more efficient in the dehydrogenation, cyclization, aromatization, etc., compared to Ru_4@HZSM-5, enabling favorable reaction dynamics in polymer upcycling toward aromatics generation. In summary, Ru_{10}@HZSM-5 exhibited superior efficiency in dehydrogenation, cyclization, and aromatization, along with optimal H* binding capacity (for hydrogenolysis) and reduced tendencies for *β*-scission and rehydrogenation, compared to Ru_4@HZSM-5. These characteristics contributed to more favorable reaction dynamics for polymer upcycling, particularly toward aromatic production (Figure 7).

Note that the Strategic Optimization of Support Acidity and Comprehensive Investigation of Practical Application Efficacy is supplemented in Supporting Information.

CONCLUSION

This study highlighted the promising potential of hydrogen- and solvent-free thermal upcycling of plastic waste using high-order Ru AC-loaded HZSM-5. The findings showed that high-order Ru ACs significantly outperformed low-order Ru ACs in both conversion (62.93% vs 41.61%) and aromatics selectivity (70.43% vs 48.43%), leading to clear economic advantages (economic profit vs economic loss).

The atomic structure of Ru ACs contributed to optimal intermediate adsorption energies, improved dehydrogenation and dehydro-aromatization abilities, reduced H* migration barriers, and suppressed rehydrogenation of aromatics and C−C cleavage (*β*-scission) while maintaining appropriate H* binding (hydrogenolysis). At the atomic and orbital levels, the increased availability of empty orbitals in Ru ACs and the favorable Ru−C interaction (bonding characteristics) enhanced the dehydro-aromatization reaction. As a result, the TOF for aromatics production from cyclohexane dehydro-aromatization increased from 296.56 $\mu M \cdot mg^{-1}$ Ru·h^{-1} for 0.2*R*/300H to 544.34 $\mu M \cdot mg^{-1}$ Ru·h^{-1} for 0.5*R*/300H.

The scalability of this approach across various metals, supports, and acids further broadened its applicability. By optimizing the metal−acid balance, the LDPE conversion improved from 62.93% to 87%, demonstrating the potential for upcycling a wide range of common plastics effectively.

This study not only emphasized the superiority of high-order Ru ACs in waste plastic upcycling but also offered valuable mechanistic insights for the design of more efficient and cost-effective catalysts. These advancements contributed to the

https://doi.org/10.1021/acscatal.5c06674
ACS Catal. 2026, 16, 2194−2208

sustainability of polymer recycling processes and aligned with global goals for sustainable development and environmental protection. Future research should focus on practical implementation to enhance the feasibility and efficiency of plastic waste upcycling technologies. Note that further exploration of nonprecious metal catalysts (e.g., Ni) is crucial,[41] as they offer a more cost-effective and sustainable alternative for hydrogen- and solvent-free processes.

■ ASSOCIATED CONTENT

Supporting Information

The Supporting Information is available free of charge at https://pubs.acs.org/doi/10.1021/acscatal.5c06674.

Details of experimental procedures, supporting data, and partial data analysis (PDF)

■ AUTHOR INFORMATION

Corresponding Authors

Wei Yu − *SEP Key Laboratory of Eco-industry, School of Resources and Civil Engineering, Northeastern University, Shenyang 110819, P. R. China*; Email: ywneuee@163.com

Haibo Li − *SEP Key Laboratory of Eco-industry, School of Resources and Civil Engineering, Northeastern University, Shenyang 110819, P. R. China*; orcid.org/0000-0003-1514-1984; Email: lihaibo@mail.neu.edu.cn

Authors

Fan Mo − *SEP Key Laboratory of Eco-industry, School of Resources and Civil Engineering, Northeastern University, Shenyang 110819, P. R. China*

Chuan Yin − *Key Laboratory of Pollution Processes and Environmental Criteria (Ministry of Education)/Tianjin Key Laboratory of Environmental Remediation and Pollution Control, Carbon Neutrality Interdisciplinary Science Center, College of Environmental Science and Engineering, Nankai University, Tianjin 300350, China*

Ting Ma − *SEP Key Laboratory of Eco-industry, School of Resources and Civil Engineering, Northeastern University, Shenyang 110819, P. R. China*

Yue Yang − *SEP Key Laboratory of Eco-industry, School of Resources and Civil Engineering, Northeastern University, Shenyang 110819, P. R. China*

Kaixuan Wang − *SEP Key Laboratory of Eco-industry, School of Resources and Civil Engineering, Northeastern University, Shenyang 110819, P. R. China*

Xi Chen − *SEP Key Laboratory of Eco-industry, School of Resources and Civil Engineering, Northeastern University, Shenyang 110819, P. R. China*

Ningqiang Zhang − *SEP Key Laboratory of Eco-industry, School of Resources and Civil Engineering, Northeastern University, Shenyang 110819, P. R. China*

Complete contact information is available at: https://pubs.acs.org/10.1021/acscatal.5c06674

Notes

The authors declare no competing financial interest.

■ ACKNOWLEDGMENTS

This work was supported by the Key Technologies Research and Development Program [Grant Number 2024YFC2909605], Shenyang Science and Technology Program [Grant Number 24-216-2-07], and Fundamental Research Funds for the Central Universities [No. N25BSS006], [No. N25ZLE003], and [No. N25XQD083]. The authors extend their gratitude to Li Meiyu (from Scientific Compass, www.shiyanjia.com) for providing invaluable assistance with the DRIFTS analysis. The authors would like to thank eceshi (www.eceshi.com) for the support of Py-IR analysis and the Applied Chemistry and Engineering Institute (Nankai University) for the instrument support of ACTEM (JEM-ARM200F). The authors would like to thank Li Jingru from SCI-GO (www.sci-go.com) for the NMR analysis.

■ REFERENCES

(1) Plastic waste is everywhere—and countries must be held accountable for reducing it. *Nature* **2023**, *619* (7969), 222−.

(2) Dong, Q.; Lele, A. D.; Zhao, X.; Li, S.; Cheng, S.; Wang, Y.; Cui, M.; Guo, M.; Brozena, A. H.; Lin, Y.; Li, T.; Xu, L.; Qi, A.; Kevrekidis, I. G.; Mei, J.; Pan, X.; Liu, D.; Ju, Y.; Hu, L. Depolymerization of plastics by means of electrified spatiotemporal heating. *Nature* **2023**, *616* (7957), 488−494.

(3) Mo, F.; Li, H.; Zhang, P.; Li, J. Orchestrating catalytic hotspots and macromolecular architectures: Molecular engineering toward zero-waste polymer circularity. *Adv. Powder Mater.* **2026**, *5*, 100357.

(4) Mo, F.; Zhou, Q.; Wang, P.; Liu, W.; Yin, C.; Hou, Z.; Xue, W.; Wang, Q.; Wang, J.; Zheng, T.; Tao, Z.; Li, X. Hydrogen/solvent-free plastic valorization via loosely coordinated ruthenium sites steering selective aromatization. *Chem. Sci.* **2025**, *16*, 16121−16136.

(5) Mo, F.; Hou, Z.; Zhou, Q.; Chen, X.; Liu, W.; Xue, W.; Wang, Q.; Wang, J.; Zheng, T.; Tao, Z. Cu-optimized long-range interaction between Co nanoparticles and Co single atoms: Improved Fenton-like reaction activity. *Sci. Bull.* **2024**, *69*, 2529−2542.

(6) Chu, M.; Tu, W.; Zhuang, Z.; Xu, P.; Weng, X.; Wang, J.; Yan, T.; Zhang, L.; Cao, M.; Zhang, L.; Lin, H.; Fan, X.; Zhang, Q.; Wang, D.; Chen, J. Efficient polyolefin upcycling over single-atom alloy catalyst. *CCS Chem.* **2024**, 1−14.

(7) Hao, J.; Wang, T.; Cai, J.; Gao, G.; Zhuang, Z.; Yu, R.; Wu, J.; Wu, G.; Lu, S.; Wang, X.; Du, M.; Wang, D.; Zhu, H. Suppression of structural heterogeneity in high-entropy intermetallics for electrocatalytic upgrading of waste plastics. *Angew. Chem., Int. Ed.* **2024**, *64*, No. e202419369.

(8) Ma, T.; Mo, F.; Li, H.; Shang, Y.; Wang, K.; Nie, X. Boosting heterogeneous advanced oxidation processes: Curvature-driven nanotube confinement catalysis. *Water Res.* **2026**, *289*, 124928.

(9) Zhou, Q.; Song, C.; Wang, P.; Zhao, Z.; Li, Y.; Zhan, S. Generating dual-active species by triple-atom sites through peroxymonosulfate activation for treating micropollutants in complex water. *Proc. Natl. Acad. Sci.* **2023**, *120* (13), No. e2300085120.

(10) Cai, G.; Lv, H.; Zhang, G.; Liu, D.; Zhang, J.; Zhu, J.; Xu, J.; Kong, X.; Jin, S.; Wu, X.; Ji, H. A volcano correlation between catalytic activity for sulfur reduction reaction and Fe atom count in metal center. *J. Am. Chem. Soc.* **2024**, *146* (19), 13055−13065.

(11) Zhang, Z.; Wang, J.; Ge, X.; Wang, S.; Li, A.; Li, R.; Shen, J.; Liang, X.; Gan, T.; Han, X.; Zheng, X.; Duan, X.; Wang, D.; Jiang, J.; Li, Y. Mixed plastics wastes upcycling with high-stability single-atom Ru catalyst. *J. Am. Chem. Soc.* **2023**, *145* (41), 22836−22844.

(12) Zhang, F.; Zeng, M.; Yappert, R. D.; Sun, J.; Lee, Y.-H.; LaPointe, A. M.; Peters, B.; Abu-Omar, M. M.; Scott, S. L. Polyethylene upcycling to long-chain alkylaromatics by tandem hydrogenolysis/aromatization. *Science* **2020**, *370* (6515), 437−441.

(13) Du, J.; Zeng, L.; Yan, T.; Wang, C.; Wang, M.; Luo, L.; Wu, W.; Peng, Z.; Li, H.; Zeng, J. Efficient solvent- and hydrogen-free upcycling of high-density polyethylene into separable cyclic hydrocarbons. *Nat. Nanotechnol.* **2023**, *18* (7), 772−779.

(14) Kresse, G.; Furthmüller, J. Efficiency of ab-initio total energy calculations for metals and semiconductors using a plane-wave basis set. *Comput. Mater. Sci.* **1996**, *6* (1), 15−50.

(15) Perdew, J. P.; Burke, K.; Ernzerhof, M. Generalized gradient approximation made simple. *Phys. Rev. Lett.* **1996**, *77* (18), 3865−3868.
(16) Blöchl, P. E. Projector augmented-wave method. *Matter Mater. Phys.* **1994**, *50* (24), 17953−17979.
(17) Kresse, G.; Joubert, D. From ultrasoft pseudopotentials to the projector augmented-wave method. *Phys. Rev. B* **1999**, *59* (3), 1758−1775.
(18) Grimme, S.; Ehrlich, S.; Goerigk, L. Effect of the damping function in dispersion corrected density functional theory. *J. Comput. Chem.* **2011**, *32* (7), 1456−1465.
(19) Henkelman, G.; Jónsson, H. Improved tangent estimate in the nudged elastic band method for finding minimum energy paths and saddle points. *J. Chem. Phys.* **2000**, *113* (22), 9978−9985.
(20) Yuan, Y.; Huang, E.; Hwang, S.; Liu, P.; Chen, J. G. Confining platinum clusters in indium-modified ZSM-5 zeolite to promote propane dehydrogenation. *Nat. Commun.* **2024**, *15* (1), 6529.
(21) Chen, X.; Peng, M.; Xiao, D.; Liu, H.; Ma, D. Fully exposed metal clusters: Fabrication and application in alkane dehydrogenation. *ACS Catal.* **2022**, *12* (20), 12720−12743.
(22) Sotoodeh, F.; Smith, K. J. Structure sensitivity of dodecahydro-N-ethylcarbazole dehydrogenation over Pd catalysts. *J. Catal.* **2011**, *279* (1), 36−47.
(23) Dong, C.; Gao, Z.; Li, Y.; Peng, M.; Wang, M.; Xu, Y.; Li, C.; Xu, M.; Deng, Y.; Qin, X.; Huang, F.; Wei, X.; Wang, Y.-G.; Liu, H.; Zhou, W.; Ma, D. Fully exposed palladium cluster catalysts enable hydrogen production from nitrogen heterocycles. *Nat. Catal.* **2022**, *5* (6), 485−493.
(24) Yao, S.; Zhang, X.; Zhou, W.; Gao, R.; Xu, W.; Ye, Y.; Lin, L.; Wen, X.; Liu, P.; Chen, B.; Crumlin, E.; Guo, J.; Zuo, Z.; Li, W.; Xie, J.; Lu, L.; Kiely, C. J.; Gu, L.; Shi, C.; Rodriguez, J. A.; Ma, D. Atomic-layered Au clusters on α-MoC as catalysts for the low-temperature water-gas shift reaction. *Science* **2017**, *357* (6349), 389−393.
(25) Hou, Z.; Mo, F.; Zhou, Q.; Xie, Y.; Liu, X.; Zheng, T.; Tao, Z. Key role of vegetation cover in alleviating microplastic-enhanced carbon emissions. *Environ. Sci. Technol.* **2024**, *58*, 3288−3301.
(26) Wang, W.; Li, C.; Zhou, C.; Xiao, X.; Li, F.; Huang, N. Y.; Li, L.; Gu, M.; Xu, Q. Enrooted-type metal-support interaction boosting oxygen evolution reaction in acidic media. *Angew. Chem., Int. Ed.* **2024**, *136* (28), No. e202406947.
(27) Chen, L.; Meyer, L. C.; Kovarik, L.; Meira, D.; Pereira-Hernandez, X. I.; Shi, H.; Khivantsev, K.; Gutiérrez, O. Y.; Szanyi, J. Disordered, sub-nanometer Ru structures on CeO_2 are highly efficient and selective catalysts in polymer upcycling by hydrogenolysis. *ACS Catal.* **2022**, *12* (8), 4618−4627.
(28) Zachariah, A.; Wang, L.; Yang, S.; Prasad, V.; de Klerk, A. Suppression of coke formation during bitumen pyrolysis. *Energy Fuels* **2013**, *27* (6), 3061−3070.
(29) Wang, B.; Froment, G. F. Dehydrogenation of cyclohexane on Pt(111) in a bulb reactor. *Catal. Lett.* **2017**, *147* (3), 663−673.
(30) Zhang, N.; Ma, J.; Li, R.; Jiao, H. Hydrocracking of fused aromatic hydrocarbons catalyzed by Al-substituted HZSM-52014A case study of 9,10-dihydroanthracene. *ACS Catal.* **2020**, *10* (16), 9215−9226.
(31) Fu, J.; Liu, S.; Zheng, W.; Huang, R.; Wang, C.; Lawal, A.; Alexopoulos, K.; Liu, S.; Wang, Y.; Yu, K.; Boscoboinik, J. A.; Liu, Y.; Liu, X.; Frenkel, A. I.; Abdelrahman, O. A.; Gorte, R. J.; Caratzoulas, S.; Vlachos, D. G. Modulating the dynamics of Brønsted acid sites on PtWOx inverse catalyst. *Nat. Catal.* **2022**, *5* (2), 144−153.
(32) Shi, H.; Li, X.; Haller, G. L.; Gutiérrez, O. Y.; Lercher, J. A. Active sites and reactive intermediates in the hydrogenolytic cleavage of C-C bonds in cyclohexane over supported iridium. *J. Catal.* **2012**, *295*, 133−145.
(33) Song, C.; Wang, M.; Zhao, L.; Xue, N.; Peng, L.; Guo, X.; Ding, W.; Yang, W.; Xie, Z. Synergism between the Lewis and Brönsted acid sites on HZSM-5 zeolites in the conversion of methylcyclohexane. *Chin. J. Catal.* **2013**, *34* (11), 2153−2159.
(34) Guo, J.; Peng, M.; Jia, Z.; Li, C.; Liu, H.; Zhang, H.; Ma, D. Kinetic evidence of most abundant surface intermediates variation over Pt_n and Pt_p: Few-atom Pt ensembles enable efficient catalytic cyclohexane dehydrogenation for hydrogen production-II. *ACS Catal.* **2022**, *12* (12), 7248−7261.
(35) Chauhan, K. Y.; Das, T. Gas phase oxidative dehydrogenation of cyclohexane over alumina-supported copper-manganese oxide catalyst: In-situ DRIFTS studies. *Chem. Eng. Sci.* **2024**, *288*, 119847.
(36) Yu, J.; Wang, R.; Ren, S.; Sun, X.; Chen, C.; Ge, Q.; Fang, W.; Zhang, J.; Xu, H.; Su, D. S. The unique role of CaO in stabilizing the Pt/Al_2O_3 catalyst for the dehydrogenation of cyclohexane. *ChemCatChem* **2012**, *4* (9), 1376−1381.
(37) Liu, Q.; Wen, M.; Guo, Y.; Song, S.; Li, G.; An, T. Efficient catalytic combustion of cyclohexane over $PdAg/Fe_2O_3$ catalysts under low-temperature conditions: Establishing the degradation mechanism using PTR-TOF-MS and *in situ* DRIFTS. *ACS Appl. Mater. Interfaces* **2022**, *14* (50), 55503−55516.
(38) Cordoba, M.; Garcia, L.; Badano, J.; Betti, C.; Coloma-Pascual, F.; Quiroga, M.; Lederhos, C. *In situ* DRIFTS analysis during hydrogenation of 1-pentyne and olefin purification with Ag nanoparticles. *ChemPlusChem* **2023**, *88* (10), No. e202300344.
(39) Asemani, M.; Rabbani, A. R. Detailed FTIR spectroscopy characterization of crude oil extracted asphaltenes: Curve resolve of overlapping bands. *J. Pet. Sci. Eng.* **2020**, *185*, 106618.
(40) Hammer, B.; Norskov, J. K. Why gold is the noblest of all the metals. *Nature* **1995**, *376* (6537), 238−240.
(41) Sun, B.; Xu, H.; Li, T.; Guan, W.; Wang, K. Hydrogen-free upcycling of polyethylene waste to methylated aromatics over Ni/ZSM-5 under mild conditions. *J. Hazard. Mater.* **2025**, *482*, 136564.

https://doi.org/10.1021/acscatal.5c06674
ACS Catal. 2026, 16, 2194−2208